Earth and Planetary Science Letters 426 (2015) 280–292

Contents lists available at ScienceDirect

Earth and Planetary Science Letters

www.elsevier.com/locate/epsl

# Predicting short-period, wind-wave-generated seismic noise in coastal regions

Florent Gimbert[a,b,*], Victor C. Tsai[a,b]

[a] Seismological Laboratory, California Institute of Technology, Pasadena, CA, USA
[b] Division of Geological and Planetary Sciences, California Institute of Technology, Pasadena, CA, USA

ARTICLE INFO

*Article history:*
Received 19 March 2015
Received in revised form 5 June 2015
Accepted 6 June 2015
Available online 7 July 2015
Editor: P. Shearer

*Keywords:*
ocean waves
seismic noise
directional spectra
wind

## ABSTRACT

Substantial effort has recently been made to predict seismic energy caused by ocean waves in the 4–10 s period range. However, little work has been devoted to predict shorter period seismic waves recorded in coastal regions. Here we present an analytical framework that relates the signature of seismic noise recorded at 0.6–2 s periods (0.5–1.5 Hz frequencies) in coastal regions with deep-ocean wave properties. Constraints on key model parameters such as seismic attenuation and ocean wave directionality are provided by jointly analyzing ocean-floor acoustic noise and seismic noise measurements. We show that 0.6–2 s seismic noise can be consistently predicted over the entire year. The seismic noise recorded in this period range is mostly caused by local wind-waves, i.e. by wind-waves occurring within about 2000 km of the seismic station. Our analysis also shows that the fraction of ocean waves traveling in nearly opposite directions is orders of magnitude smaller than previously suggested for wind-waves, does not depend strongly on wind speed as previously proposed, and instead may depend weakly on the heterogeneity of the wind field. This study suggests that wind-wave conditions can be studied in detail from seismic observations, including under specific conditions such as in the presence of sea ice.

## 1. Introduction

Ocean waves generate seismic waves either directly by interacting with the shoreline (primary microseisms, Hasselmann, 1963; Ardhuin et al., 2015) or indirectly through wave–wave interactions (secondary microseisms, Longuet-Higgins, 1950; Hasselmann, 1963; Ardhuin et al., 2013). It is well known that these two different processes cause two distinct peaks in seismic noise spectra with maximum amplitudes at periods of 8–16 s for primary microseisms and of 4–8 s for secondary microseisms (McNamara and Buland, 2004; Berger et al., 2004).

Microseisms are particularly useful for studying Earth structure using noise cross correlation techniques (Campillo and Paul, 2003; Bowden et al., 2015), and better knowledge of their characteristics is needed to avoid spurious artifacts caused by spatial and temporal variations in noise sources (Tsai, 2009; Fichtner, 2014). Numerous investigations have been conducted to better understand the ocean processes that create microseismic noise and their spatiotemporal characteristics. Maximum amplitudes of the secondary microseism peak (4–8 s) have been successfully predicted (Kedar et al., 2008; Ardhuin et al., 2015) by combining numerical ocean wave models with the Longuet-Higgins (LH) theory (Longuet-Higgins and Ursell, 1948; Longuet-Higgins, 1950), as later revisited by Hasselmann (1963). The maximum energy in that period range is mainly caused by strong ocean swell populations with periods of typically 8–16 s, i.e. wavelengths of 100–400 m, that travel in nearly opposite directions either in coastal or deep-ocean regions as a result of their generation by distant storms, by single but fast moving storms or by coastline reflections.

In contrast to these previous findings, little attention has been devoted to understanding how ocean processes cause the relatively shorter period (<4 s) seismic noise discussed in various recent studies (Zhang et al., 2009; Tsai and McNamara, 2011; Beucler et al., 2014). In contrast to the longer (4–8 s) periods at which secondary microseisms are observed almost everywhere in continental areas (Berger et al., 2004), shorter period ocean-induced noise is expected to be more restricted to coastal regions since seismic waves are more attenuated at these shorter periods. However, short-period ocean noise is increasingly used for high-resolution imaging of shallow Earth structure in coastal regions (Lin et al., 2013; Bowden et al., 2015). Moreover, Tsai and McNamara (2011) suggested that sea-ice mechanical properties could be continuously monitored from the analysis of coastal ground mo-

---

* Corresponding author.
*E-mail address:* flo.gimbert1754@gmail.com (F. Gimbert).

http://dx.doi.org/10.1016/j.epsl.2015.06.017

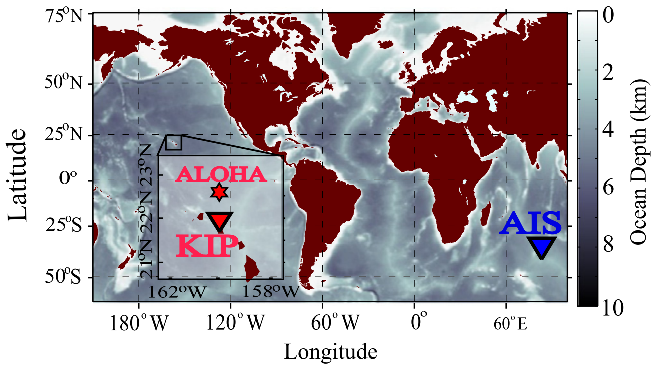

**Fig. 1.** Locations of the seismic stations KIP and AIS (triangles) and the marine hydrophone station ALOHA (star) used in this study. The color scale indicates ocean depth. (For interpretation of the references to color in this figure legend, the reader is referred to the web version of this article.)

tion in the 0.6–2 s period band. Before such a goal can be achieved, though, an accurate understanding of coastal seismic noise amplitude and frequency scaling under sea-ice free conditions is needed: this is the main purpose of this study.

As in Webb (1992), Farrell and Munk (2008) and Duennebier et al. (2012), we adopt a simple analytical approach that predicts secondary microseisms from the interaction of short-wavelength (1–25 m) wind-waves. In contrast to these previous studies who limited their analysis to the modeling of acoustic pressure and ground floor displacement at the ocean bottom, we conjointly model pressure spectra recorded at the ocean bottom together with acceleration spectra recorded by seismic stations in coastal areas. This joint analysis allows us to independently constrain the key ocean-wave and seismic model parameters through their control on the amplitude and variability of acoustic and seismic noise records.

## 2. Data

We use seismic data from the 2 stations KIP (Oahu, Hawaii; Pacific Ocean) and AIS (Amsterdam Island; Indian Ocean) shown in Fig. 1. For simplicity, we only consider these two island stations surrounded by 4–6 km deep ocean, where model predictions are relatively insensitive to uncertainties in ground properties (see Section 3.2.2). However, we also expect our modeling framework to apply to continental stations with shallow ocean nearby.

Acoustic noise records are taken from Duennebier et al. (2012), who reported broadband hydrophone measurements at the ALOHA Cabled Observatory, 100 km north of Oahu, Hawaii (see red star in Fig. 1). This station is located near the KIP seismic station, so that our acoustic and seismic noise predictions can be done jointly at this location. Details on the deployment and signal acquisition at station ALOHA are provided by Duennebier et al. (2008, 2012). We use frequency spectra that were processed by Duennebier et al. (2012) over the 20 months of continuous acoustic noise records acquired from February 2007 to October 2008. As in Duennebier et al. (2012), we consider average spectra that have been sorted by local-wind speed, which was independently measured above the ALOHA station by the WHOTS meteorological buoy (see Plueddemann et al., 2006).

We use estimates of near-surface wind speeds provided by the ERA-Interim dataset of the ECMWF (Dee et al., 2011). This model simulation includes 12-h assimilations of observations with 3-hourly model outputs on a regular grid with a 0.7° horizontal resolution. Finally, for ocean depths, we use the bathymetry map ETOPO2 provided by the NOAA data center (http://www.ngdc.noaa.gov) with a 2-minute latitude and longitude resolution.

## 3. Model

In this section, we calculate the ground acceleration power spectral density (PSD) $A(f_s)$ defined at seismic frequency $f_s$ and over a given time window of duration $T$ as

$$A(f_s) = \frac{1}{T}\left(\int_0^T a(t)e^{-2\pi i f_s t}dt\right)^2 \tag{1}$$

where $a(t)$ is the ground acceleration timeseries. For the $<4$ s periods of interest, the ocean surface gravity waves (OSGW) that cause the observed ground motion have wavelengths ($<25$ m) that are much shorter than ocean depths such that the deep water approximation is appropriate. For such 'deep water' conditions, ocean-surface pressure fluctuations are thought to generate seismic surface waves only from the interaction of OSGW pairs. Any interacting OSGW pairs with wavenumber vectors $\mathbf{k}$ and $\mathbf{k}'$, and associated frequencies $f$ and $f'$, generate a resultant wave of horizontal wave number $\mathbf{K} = \mathbf{k} + \mathbf{k}'$. Of all wave types resulting from all possibly interacting OSGW pairs, only those that satisfy $|\mathbf{K}| \approx 0$, i.e. $\mathbf{k} \approx -\mathbf{k}'$, and consequently $f \approx f'$ contribute to seismic wave generation in deep water (Longuet-Higgins, 1950; Hasselmann, 1963; Ardhuin and Herbers, 2013). The frequency of the surface forcing is $f_s = f + f' \approx 2f$ and its amplitude is proportional to the amplitude and fraction of nearly-oppositely traveling wave pairs within the broad OSGW spectrum $E(f,\theta) = E(f)M(f,\theta)$ (with dimension $\mathrm{m}^2\,\mathrm{Hz}^{-1}$), where $E(f)$ is the ocean surface wave elevation PSD and $M(f,\theta)$ is the directional distribution of OSGWs that depends on azimuth $\theta$, and satisfies $\int_{-\pi}^{\pi} M(f,\theta)d\theta = 1$ (Mitsuyasu et al., 1975; Ewans, 1998). The fraction of interacting wave pairs can be represented by the overlap function $I(f)$ defined as

$$I(f) = \int_0^{\pi} M(f,\theta)M(f,\theta+\pi)d\theta, \tag{2}$$

so that the PSD $P(\mathbf{K} \approx 0, f_s)$ of pressure fluctuations in frequency-2 dimensional (2D) wavenumber space (with dimension $\mathrm{N}^2\,\mathrm{m}^{-2}\,\mathrm{Hz}^{-1}$, see Hasselmann, 1963) can be approximated around $\mathbf{K} \approx 0$ as (Ardhuin et al., 2013)

$$P(\mathbf{K} \approx 0, f_s) \approx \rho_w^2 g^2 f_s E^2(f_s/2) I(f_s/2) \tag{3}$$

where $g$ is the gravitational acceleration and $\rho_w$ is water density.

We assume that seismic energy is dominated by seismic surface waves, and we thus neglect the contribution of direct P and S waves. This assumption is appropriate for coastal stations that are mainly sensitive to local oceanic sources (Ardhuin and Herbers, 2013), but would be less appropriate for farther-inland stations, where P and S waves can significantly contribute to the observed noise (Zhang et al., 2009). As in Gualtieri et al. (2013), we integrate the contribution of pressure fluctuations resulting from all interacting OSGW pairs within the area $\Gamma_i$ of each element number $i$ of the wind grid by considering an equivalent point force acting in its center $\mathbf{x}_i$. The equivalent point force PSD $F_i(f_s)$ (with dimension $\mathrm{N}^2\,\mathrm{Hz}^{-1}$) resulting from the pressure PSD $P_i(\mathbf{K} \approx 0, f_s)$ can be written as

$$F_i(f_s) = 4\pi^2 P_i(\mathbf{K} \approx 0, f_s)\Gamma_i \tag{4}$$

where the $4\pi^2$ pre-factor results from the conversion from the 2D wavenumber to the 2D spatial domain. The total PSD of the vertical acceleration of the ocean floor $A^{of}(f_s, \mathbf{x}, H)$ at horizontal coordinate $\mathbf{x}$ and at depth $H$ where $H$ is the ocean layer thickness can be calculated by summing all surface-wave modes and cell contributions as (Aki and Richards, 2002)

$$A^{of}(f_s,\mathbf{x},H)=\sum_{j=1}^{\infty}A_j^{of}(f_s,\mathbf{x},H)$$
$$=(2\pi f_s)^4\sum_{i=1}^{N_{cell}}F_i(f_s)$$
$$\times\sum_{j=1}^{\infty}G_j\Big(f_s,(\mathbf{x},H);(\mathbf{x}_i,0)\Big)^2 \qquad (5)$$

where $A_j^{of}(f_s,\mathbf{x},H)$ is the PSD of ocean floor acceleration in the vertical direction for mode $j$ surface waves, $G_j\Big(f_s,(\mathbf{x},H);(\mathbf{x}_i,0)\Big)$ is the vertical displacement Green's function at $(\mathbf{x},H)$ for a vertical point force at the ocean surface $(\mathbf{x}_i,0)$, $N_{cell}$ is the number of grid cells in ocean-covered areas and the prefactor $(2\pi f_s)^4$ results from converting displacement to acceleration power.

The PSD $A^c(f_s,\mathbf{x},0)$ of ground acceleration in continental regions likely differs from that defined above for ocean floor acceleration because (i) displacement is no longer evaluated underwater (at depth $H$) but rather at the surface (Tanimoto, 2013), (ii) the seismic structure of continental crust is expected to differ from that of oceanic crust, (iii) wave scattering and seismic energy loss is expected at the ocean–continent boundary due to a relatively sharp change of topography and structure there (McGarr, 1969), and (iv) seismic wave attenuation is expected to be larger in continental areas than in ocean-covered areas (regardless of changes in crustal structure), since seismic surface waves in ocean-covered areas propagate partly in water and anelastic attenuation is much smaller for water than for rocks (Gualtieri et al., 2013). For simplicity, hereafter we only account for (iv) in our model, and we later discuss in Section 6.1 the potential prediction bias resulting from neglecting the other points. With this simplification, analytical expressions for the PSDs $A^{of}(f_s)$ and $A^c(f_s)$ are provided below by first defining the ocean surface wave elevation PSD $E(f)$ (which is needed to calculate the PSD $F(f_s)$, see equations (3) and (4)) and the appropriate Green's functions for oceanic and continental situations.

### 3.1. *The surface wave elevation spectrum*

OSGW amplitudes depend on wind speed, wind duration, fetch, wave–wave interactions, wave breaking and the presence of swell. As discussed in the introduction, ocean swell causes seismic noise at longer periods than those of interest here (Kedar et al., 2008; Ardhuin et al., 2015). Thus, we restrict our analysis to wind-waves, i.e. waves that are set by the local wind. Fetch distance and wind duration are major controls on the development and amplitude of those waves (Pierson and Moskowitz, 1964). For large enough fetch distances and long enough wind durations, though, wind waves eventually reach their fully developed stage, i.e. their amplitudes saturate at all frequencies down to a peak frequency $f_p$ at which the wave velocity approaches the wind velocity. Following Alves et al. (2003), we estimate $f_p \approx 0.159gU_{10}^{-1}$, where $U_{10}$ is the wind velocity 10 m above sea level. Fully developed waves are expected for fetch distances larger than about 8 km and 600 km, respectively, for the wind-speed extrema of 2 m/s and 18 m/s considered later (Holthuijsen, 2010). These minimum fetch distances for fully developed waves correspond to minimum wind durations (for the $f_p$ frequency wave to travel the minimum fetch distance) of about 1 h for 2 m/s wind speeds and about 10 h for 18 m/s wind speeds. We assume that fully developed waves always occur and we discuss the potential model prediction bias due to this assumption in Sections 5 and 6.1.

An expression for the fully developed OSGW spectrum was first proposed by Phillips (1958), who suggested that the maximum amplitude of the OSGW spectrum is controlled by wave breaking, and is thus unlikely to depend on near-surface wind speeds. From dimensional arguments, Phillips (1958) proposed that the surface elevation spectrum $E(f)$ scales as $g^2f^{-5}$, which has since been referred to as saturation-range scaling (see Fig. 2). While the seminal paper of Pierson and Moskowitz (1964) first showed good agreement between Phillip's saturation-range scaling and observations, other studies later suggested that there exists a frequency range, often referred to as the equilibrium range, for which the amplitude spectrum deviates from an $f^{-5}$-dependence and is a function of near-surface wind speed such that $E(f)$ rather scales as $U_{10}gf^{-4}$ (Mitsuyasu et al., 1975; Forristall, 1981; Kahma, 1981; Kitaigorodskii, 1983; Donelan et al., 1985; Long and Resio, 2007). More recently, Battjes et al. (1987) and Alves et al. (2003) revisited the database of Pierson and Moskowitz (1964) and concluded that the $f^{-4}$-scaling of the equilibrium range captures the observations better than an $f^{-5}$-scaling does in the frequency range that they investigated, i.e. between $1.5f_p$ and $4f_p$.

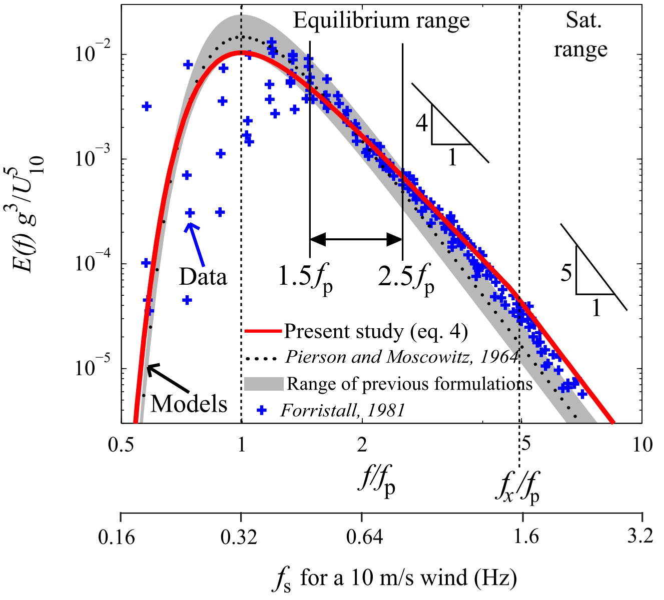

**Fig. 2.** Unidirectional OSGW elevation spectrum $E(f)$ used in this study (thick red line) as a function of non-dimensional frequency $f/f_p$. The blue crosses correspond to the data analyzed by Forristall (1981). The dotted line shows the classical $f^{-5}$ Pierson–Moskowitz (PM) spectrum built on Phillip's saturation-range scaling. The gray region shows the potential deviations from the PM spectrum discussed by Hasselmann et al. (1976) and Kahma (1981). The second $x$-axis provides the seismic frequencies to which this spectrum corresponds for a wind speed of 10 m/s. (For interpretation of the references to color in this figure legend, the reader is referred to the web version of this article.)

Such an $f^{-4}$-scaling for the wind–sea spectrum has also been theoretically supported by Kitaigorodskii (1983). Based on Hasselmann's previous work on non-linear wave–wave interactions (Hasselmann, 1962) and assuming a spectral energy influx from wind that is concentrated relatively close to the peak spectrum, i.e. concentrated at low frequencies, Kitaigorodskii (1983) showed that a Kolmogorov-like transfer of energy from low to high frequencies by wave interactions in the deep ocean causes the surface elevation spectrum to scale with frequency as $f^{-4}$ within that range. This equilibrium range extends from the peak frequency up to the cut-off frequency $f_x$ at which the sea surface acceleration reaches the limit for wave breaking, which Phillips (1958) hypothesized to correspond to the downward gravitational acceleration $g$ (see Fig. 2). Above the cut-off frequency $f_x$, Phillip's saturation range is expected. Kitaigorodskii (1983) roughly estimated the non-dimensional equilibrium-range frequency cut-off $\tilde{f}_x = f_xU_{10}/g$ to be at most ≈0.25–0.5.

We interpret the abrupt change in the frequency scaling of the acoustic power spectra reported by Duennebier et al. (2012) at ALOHA (see Fig. S1(a)) to be due to the transition from Kitaigorodskii's equilibrium range to Phillip's saturation range. We infer $\tilde{f}_x$ by reporting the cut-off frequency values observed at ALOHA as a function of wind speed. We find $\tilde{f}_x = 0.75$ (see Fig. S1(b)) and use this value throughout. This value is of the same order as those observed by Forristall (1981) ($\tilde{f}_x \approx 0.65$ for wind speeds varying from 0 to 28 m/s) and Long and Resio (2007) ($f_x \approx 2.1 - 3.5 f_p$, i.e. $\tilde{f}_x = 0.33 - 0.56$, for wind speeds varying from 2 to 24.5 m/s) and discussed by Kahma (1981) ($\tilde{f}_x \approx 0.8$) and Hwang and Wang (2001) ($f_x \approx 2.1$–$2.9 f_p$, i.e. $\tilde{f}_x \approx 0.33$–$0.46$).

Thus, we use an $f^{-4}$-scaling for $E(f)$ to describe the equilibrium range from the peak frequency $f_p$ up to $f_x$, and include a saturation range with an $f^{-5}$-scaling at higher frequencies. By imposing continuity of the spectrum at $f_x$, we write $E(f)$ as

$$\begin{aligned} E(f) &= \gamma U_{10} g f^{-4} \exp\left[ -\left( \frac{f}{f_p} \right)^{-4} \right] && \text{for} \quad f < \frac{g}{U_{10}} \tilde{f}_x \\ E(f) &= \tilde{f}_x \gamma g^2 f^{-5} && \text{for} \quad f \geq \frac{g}{U_{10}} \tilde{f}_x, \end{aligned} \tag{6}$$

where $\gamma$ is a constant and the exponential term accounts for a frequency cut-off at $f_p$. By adjusting the $f^{-5}$-scaling of the form $\gamma' g^2 (2\pi f)^{-5}$ to fit observations, Phillips (1958) originally suggested that $\gamma' = 0.0074$ was a universal constant. Pierson and Moskowitz (1964) later obtained $\gamma' = 0.0081$ from fitting the observations of the Joint North Sea Wave Project, and proposed the classical Pierson–Moskowitz (PM) spectrum shown by the dotted line in Fig. 2. Since then, other investigators have shown that $\gamma'$ is in fact not a universal constant and may vary by about a factor of 2 depending on situations (e.g., Hasselmann et al., 1976; Kahma, 1981). The range of ocean wave spectra for these expected $\gamma'$-variations is shown by the gray regions in Fig. 2. It is important to note that the $\gamma'$-values and thus the gray region in Fig. 2 were constrained by adjusting the $f^{-5}$ ocean wave spectrum scaling to match observations only in the relatively low frequency range of $1.5 f_p$ to $2.5 f_p$ (Phillips, 1958; Pierson and Moskowitz, 1964; Hasselmann et al., 1976).

We determine the constant $\gamma$ of equation (6) so that it agrees with the amplitude of previously proposed formulations in the $1.5 f_p$–$2.5 f_p$ frequency range (see Fig. 2). We use $\gamma = 1.8 \cdot 10^{-5}$ and obtain the OSGW spectrum shown by the red line in Fig. 2. Our result as well as the observations of Forristall (1981) (see blue crosses in Fig. 2) roughly agree with previous parameterizations in the $1.5 f_p$ to $2.5 f_p$ frequency range, but deviate from the later at larger frequencies as a result of an $f^{-4}$ rather than $f^{-5}$-scaling for frequencies lower than $f_x$. Accounting for these differences in scaling and amplitude of the omnidirectional spectrum with respect to the classical PM spectrum has important implications at the higher frequencies of $2 f_p$ to $5 f_p$ (0.5 to 1.5 Hz for 10 m/s wind speeds, see Fig. 2) that we mostly investigate here. In particular, we show that the use of this modified $f^{-4}$-scaling strongly affects the overlap function $I$ inferred from acoustic and seismic observations.

### *3.2. Acoustic and seismic noise*

#### *3.2.1. The acoustic spectrum*

Ocean-floor acoustic measurements are affected by direct acoustic waves propagating down the water column and by pressure fluctuations resulting from seismic waves excited by more distant seas (Ardhuin and Herbers, 2013). The PSD $P_D^a(f_s)$ of directly created acoustic pressure can be obtained following Ardhuin and Herbers (2013) by integrating the contribution of all waves with a non-zero down-propagating component in the water column, i.e. all waves that satisfy $|\mathbf{K}| < 2\pi f_s/\alpha_w$. To do this, the pressure PSD $P(\mathbf{K} \approx 0, f_s)$ of equation (3) is integrated within the circle of radius $2\pi f_s/\alpha_w$ in 2D-wavenumber space to obtain

$$P_D^a(f_s) \approx \pi \frac{(2\pi f_s)^2}{\alpha_w^2} \rho_w^2 g^2 f_s E^2(f_s/2) I(f_s/2), \tag{7}$$

where $\alpha_w = 1500$ m/s is the sound speed in water.

The PSD $P_I^a(f_s, \mathbf{x}, z)$ of acoustic pressure at depth $z$ below the water surface resulting indirectly from more distant seas through ocean floor shaking at location $\mathbf{x}$ can be evaluated by solving for mode resonance in the water column. The pressure $p(z)$ equals the water stiffness $K_w$ times the strain $l_j \delta$ due to the acoustic wave, where $\delta$ is the ocean floor displacement and $l_j = 2\pi f_s \sqrt{\frac{1}{\alpha_w^2} - \frac{1}{v_j^2}}$ is the vertical wave number of the mode $j$ surface wave propagating at horizontal phase velocity $v_j$. By using the sound wave relation $\alpha_w = \sqrt{K_w/\rho_w}$ and applying boundary conditions of zero pressure at the ocean surface (free surface) and predicted displacement at the ocean bottom, one can express $P_i^a(f_s)$ as a function of the ocean-floor acceleration PSD $A_j^{of}(f_s, \mathbf{x}, H)$ as (Ardhuin et al., 2013)

$$P_I^a(f_s, \mathbf{x}, z) = \sum_{j=1}^{\infty} \left[ \rho_w \frac{\sin(l_j z)}{l_j \cos(l_j H)} \right]^2 A_j^{of}(f_s, \mathbf{x}, H). \tag{8}$$

The final PSD $P^a(f_s)$ of acoustic pressure at the hydrophone may be calculated as $P^a(f_s) = P_D^a(f_s) + P_I^a(f_s)$, and thus involves the independent calculation of ocean-floor acceleration power $A_j^{of}(f_s)$, which is performed in the following section.

#### *3.2.2. The ocean floor acceleration spectrum*

In order to calculate the PSD $A_j^{of}$ of vertical ocean floor acceleration due to mode $j$ surface waves (see equation (5)), we express the vertical–vertical Rayleigh-wave Green's function $G_j$ as (Aki and Richards, 2002)

$$G_j\Big(f_s, (\mathbf{x}, H); (\mathbf{x}_i, 0)\Big) = \frac{r_j^v(0) r_j^v(H)}{8 u_j v_j \mathbb{I}_{1j}} \sqrt{\frac{2}{\pi k_j d_i}} e^{-\pi f_s d_i/(u_j Q)} \tag{9}$$

where $r_j^v(H)$ and $r_j^v(0)$ are the vertical eigenfunctions of the mode $j$ surface wave at the ocean bottom and at the ocean surface, respectively, $u_j$ and $v_j$ are the group and phase velocities, $k_j = 2\pi f_s/v_j$ is the horizontal wavenumber, $Q$ is the quality factor that we assume to be mode independent, $d_i = |\mathbf{x} - \mathbf{x}_i|$ is the lateral source-to-station distance and $\mathbb{I}_{1j} = 1/2 \int_0^\infty \rho(z)[r_j^h(z)^2 + r_j^v(z)^2] dz$ is the integral of horizontal $r_j^h$ and vertical $r_j^v$ displacement eigenfunctions with depth $z$, $\rho(z)$ being either equal to $\rho_w$ in the ocean, $\rho_s$ in the sediments or $\rho_c$ in the crust. The general Green's function expression as defined in equation (9) can be mapped to that originally proposed by Longuet-Higgins (1950, see equation (183) therein) by taking the ocean crust of uniform density $\rho_c$ and shear-wave speed $\beta_c$ as a reference, and rewriting equation (9) as

$$G_j\Big(f_s, (\mathbf{x}, H); (\mathbf{x}_i, 0)\Big) = f_s \frac{c_j}{\rho_c \beta_c^{5/2}} \sqrt{\frac{1}{d_i}} e^{-\pi f_s d_i/(u_j Q)} \tag{10}$$

where

$$c_j = \frac{N_j(H, 0) \beta_c^{5/2}}{4 u_j v_j^{3/2}} \tag{11}$$

and $N_j(H, 0)$ is defined as in Tsai and Atiganyanun (2014) as

$$N_j(H, 0) = \frac{\rho_c r_j^v(0) r_j^v(H)}{k_j \mathbb{I}_{1j}}. \tag{12}$$

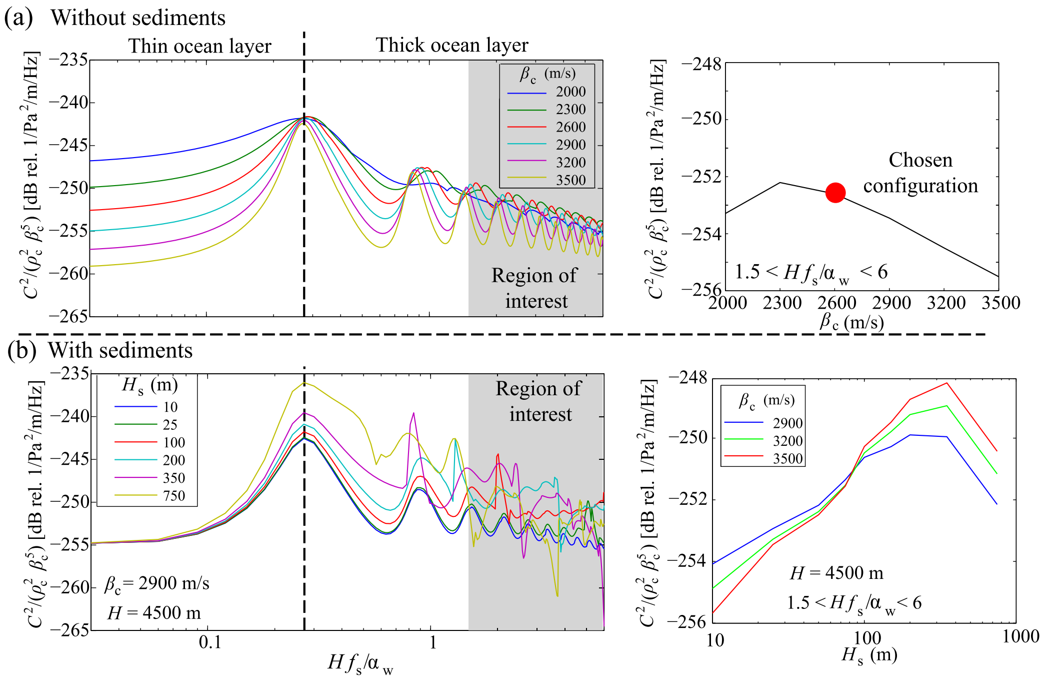

**Fig. 3.** Green's function pre-factor $C^2/(\rho_c^2\beta_c^5)$ (see equation (13), summed over all modes) for an ocean layer (a) over a homogeneous half-space with various shear-wave speeds $\beta_c$ and (b) over a sedimentary layer of depth-average shear-wave speed $\beta_s$ on top of a homogeneous half-space with various shear-wave speeds $\beta_c$. We use $\rho_c = 2500$ kg/m$^3$, $\rho_s = 1700$ kg/m$^3$, $\alpha_c = \sqrt{3}\beta_c$ and $\alpha_s = 1500$ m/s. Left panels show $C^2/(\rho_c^2\beta_c^5)$ as a function of dimensionless frequency $Hf_s/\alpha_w$, with the gray zones delimiting the region of interest in this study given an ocean depth range that mainly varies between 4000 and 6000 m around KIP and AIS (see Fig. 1) and a frequency range of interest varying between 0.5 and 1.5 Hz. The average values of the pre-factor $C^2/(\rho_c^2\beta_c^5)$ within the grey regions are shown in the right panels as a function of (a) $\beta_c$ and (b) $H_s$ for various values of $\beta_c$.

By substituting the Green's function of equation (10) into the definition of the total PSD $A^{of}(f_s, \mathbf{x}, H)$ provided in equation (5), one can rewrite $A^{of}(f_s, \mathbf{x}, H)$ as in Ardhuin and Herbers (2013) by assuming that all modes propagate at the same group velocity $u$ so that

$$A^{of}(f_s, \mathbf{x}, H) = (2\pi f_s)^4 \sum_{i=1}^{N_{cell}} T_i(f_s)\frac{1}{d_i} e^{-2\pi f_s d_i/(uQ)} \qquad (13)$$

where

$$T_i(f_s) = f_s \frac{C^2}{\rho_c^2\beta_c^5} F_i(f_s) \qquad (14)$$

and $C = \sqrt{\sum_{j=1}^{\infty} c_j^2}$ are coefficients.

### *3.2.3. Sensitivity of ground motion to ground properties*

We evaluate the sensitivity of ground motion amplitude to ground properties by calculating the Green's function pre-factor $C^2/(\rho_c^2\beta_c^5)$ for different structures. We first consider the case of a water layer on top of the crust as an 'equivalent' homogeneous half-space (i.e. no explicit sediment layer) of constant density $\rho_c = 2.5$ kg/m$^3$ and different constant shear and compressional wave speeds $\beta_c$ and $\alpha_c = \sqrt{3}\beta_c$ where $\beta_c$ is varied from 2 to 3.5 km/s (see Fig. 3, in which $C$ is calculated by solving equation (179) of Longuet-Higgins, 1950). At small values of $Hf_s/\alpha_w$, i.e. for a relatively thin ocean layer, $C^2/(\rho_c^2\beta_c^5)$ strongly depends on $\beta_c$. In contrast, due to surface waves being more sensitive to the water layer for relatively deeper oceans, $C^2/(\rho_c^2\beta_c^5)$ is less sensitive to $\beta_c$ as $Hf_s/\alpha_w$ increases. In the special case of high-frequency noise at island stations surrounded by a deep ocean ($f_s \approx 0.5$–$1.5$ Hz and $H \approx 4$–$6$ km, see grey region in Fig. 3(a)), uncertainties in $\beta_c$ only causes a ±1.5 dB bias in model predictions (see right panel of Fig. 3(a)).

Next, we investigate the role of an explicit sedimentary layer of constant and uniform density $\rho_s = 1.7$ kg/m$^3$ and compressional wave speed $\alpha_s = 1.5$ km/s but varying thickness $H_s$ and depth-averaged shear-wave speed $\beta_s$. To do this, we solve for the coefficients $c_j$ as defined in equation (11) by calculating $N_{22}^j(H, 0)$ (see equation (12)), $v_c^j$ and $v_u^j$ using the numerical code provided by Herrmann (2013). In this situation, a more realistic crustal range is used for $\beta_c$ (2.9 to 3.5 km/s) and $\beta_s$ is averaged for values of $H_s$ varying from 10 m ($\beta_s = 162$ m/s) to 750 m ($\beta_s = 757$ m/s) using the generic shear-wave-speed depth profile of Hamilton (1976). An example of the variation of $C^2/(\rho_c^2\beta_c^5)$ with $Hf_s/\alpha_w$ for various $H_s$-values (and thus various $\beta_s$-values) is shown in Fig. 3(b) using $\beta_c = 2.9$ km/s and $H = 4.5$ km. As already noted by Ardhuin et al. (2013), the sediment layer modifies the amplitude and shape of each mode, causing the $C$-coefficients to exhibit a more complex variation with frequency. However, the average values of the pre-factor $C^2/(\rho_c^2\beta_c^5)$ remain of the same order of magnitude as those obtained without an explicit sediment layer. In the following, we consider the simple situation of no sediment layer and an 'equivalent' homogeneous crust of shear velocity $\beta_c = 2.6$ km/s. We note that uncertainties in ground structure cause a −3 dB to a +4 dB uncertainty in model predictions (see right panels of Fig. 3(b)).

### *3.2.4. The acceleration spectrum in continental regions*

To predict ground acceleration power in continental regions, we define two distinct quality factors $Q_w$ for water-covered areas and $Q_g$ for grounded areas and write the PSD $P_a^c$ as

$$A^c(f_s, \mathbf{x}, 0) = (2\pi f_s)^4 \sum_{i=1}^{N_{cell}} \frac{T_i(f_s)}{d_i^{sc} + d_i^{cs}} \times \exp\left(-2\pi f_s\left(\frac{d_i^{sc}}{uQ_w} + \frac{d_i^{cs}}{uQ_g}\right)\right), \qquad (15)$$

where $d_i^{sc}$ is the source-to-coast distance and $d_i^{cs}$ is the coast-to-station distance along the considered ray path. Here, we assume that seismic surface waves propagate at the same group velocity $u$ over water-covered and inland regions. In reality, the velocity of seismic waves is significantly affected by the presence or absence of the water layer on top of the crust. Tsai and Atiganyanun (2014) suggested that group velocities of fundamental-mode Rayleigh waves vary from 1 to 2 km/s for generic continental crust and in the frequency range of interest. In water-covered areas and for the crust as an 'equivalent' homogeneous half-space, group velocities may vary between $\alpha_w$ and $\beta_c$ depending on wave mode and ocean depth (e.g., see Ardhuin and Herbers, 2013). For simplicity, we approximate $u$ by $\alpha_w$, and note that this assumption could lead to at most a factor of 2 overestimate of the absolute values of $Q_w$ and $Q_g$ (compared to using $u \approx \beta_c$) inferred in the following (see Section 4), and would not change the final predictions.

The final expression for the ground acceleration power $A^c$ is obtained by substituting the expression for $T_i$ in equation (14) into equation (15). Using equations (3) and (4) to express the point force PSD $F_i(f_s)$ and equation (6) to express the OSGW spectrum $E(f)$, we obtain

$$A^c(f_s, \mathbf{x}, 0) = \sum_{i=1}^{N_{cell}} A_i^c(f_s, \mathbf{x}, 0) \tag{16}$$

where

$$\begin{aligned} A_i^c(f_s, \mathbf{x}, 0) &= \frac{\rho_w^2}{\rho_s^2}\frac{C^2}{\beta_c^5}\frac{\gamma_4^a g^4 U_{10,i}^2 I f_s^{-2}}{d_i^{sc}+d_i^{cs}}\Gamma_i \exp\left[-\left(\frac{f_s}{2f_p}\right)^{-4}\right] \\ &\quad \exp\left[-2\pi f_s\left(\frac{d_i^{sc}}{uQ_w}+\frac{d_i^{cs}}{uQ_g}\right)\right] \quad \text{if} \quad f_s < \frac{2g}{U_{10,i}}\tilde{f}_x \\ A_i^c(f_s, \mathbf{x}, 0) &= \frac{\rho_w^2}{\rho_s^2}\frac{C^2}{\beta_c^5}\frac{\gamma_5^a g^6 I f_s^{-4}}{d_i^{sc}+d_i^{cs}}\Gamma_i \\ &\quad \exp\left[-2\pi f_s\left(\frac{d_i^{sc}}{uQ_w}+\frac{d_i^{cs}}{uQ_g}\right)\right] \quad \text{if} \quad f_s \geq \frac{2g}{U_{10,i}}\tilde{f}_x \end{aligned} \tag{17}$$

using $\gamma_4^a = 4\pi^2(2\pi)^4 2^8 \gamma^2 = 5.1 \cdot 10^{-3}$ and $\gamma_5^a = 4\pi^2(2\pi)^4 \times 2^{10}\tilde{f}_x^2\gamma^2 = 1.1 \cdot 10^{-2}$.

Our model predictions use a downscaled version of the bathymetry grid (8-minute resolution) on which the coarser wind field has interpolated. This relatively high-resolution grid is particularly suitable for representing coast-to-station distances over which significant attenuation occurs at the frequencies of interest (see Section 4). The acoustic pressure power $P^a$ is calculated by summing the direct acoustic wave contributions (see equation (7)) and the contribution from ocean floor shaking (see equation (8)). The ocean floor acceleration PSD $A^{of}$ is obtained by propagating the modes separately from each grid source to the hydrophone and then stacking all mode contributions. The total ground acceleration PSD $A^c$ at a seismic station is obtained by evaluating equation (16). Prior to showing model predictions against observations in Section 5, we first provide constraints on model parameters in the next section.

## 4. Constraints on model parameters

Here we provide constraints on the overlap function $I$ and the two quality factors $Q_w$ and $Q_g$ (see equations (8) and (17)) from the joint analysis of seismic and acoustic observations at various local wind speeds. Since ocean-floor acoustic measurements are not sensitive to the inland quality factor $Q_g$ while seismic measurements are, the joint analysis of seismic and acoustic data provide useful constraints on $Q_g$. In contrast, the 2 other parameters $I$ and $Q_w$ affect the seismic and acoustic noise records similarly, since ocean-floor acoustic measurements are also mainly sensitive to distant sources through surface wave propagation (Ardhuin et al., 2013). However, the respective role of the 2 parameters $I$ and $Q_w$ in setting the resulting noise power depends on the different wind-field situations. By controlling the contribution of nearby vs. faraway sources, $Q_w$ strongly influences the predicted noise power when local wind speeds are low but distant wind speeds are higher. On the other hand, the noise power predicted when local wind speeds are strong is only weakly affected by $Q_w$, since the main noise contribution in that case comes from surface waves that propagate over short distances and thus undergo little anelastic attenuation. In this case, the acoustic power is almost entirely set by $I$.

We therefore model acoustic and seismic PSDs that we bin averaged by local wind speed. We do this jointly at KIP and ALOHA, and separately at AIS. We use the wind measurements of the WHOTS buoy as the local wind-speed reference for KIP and ALOHA, while for AIS we use wind speed at the closest grid-point of the ERA-Interim dataset (located 35 km from the station). Wind bins of 0.5 m/s are used within the 2 to 14 m/s range for KIP and ALOHA, while wind bins of 1 m/s are used within the 2 to 18 m/s range for AIS. Average PSDs for each wind bin are directly taken from Duennebier et al. (2012) for acoustic records at ALOHA, and are processed over the same time period (Feb. 2007 to Oct. 2008) for ground acceleration at KIP. The entire year of 2012 is considered for AIS. To avoid potential contamination of the observed PSDs by anthropogenic noise sources at KIP (see Fig. S2), PSDs and wind fields are only taken from night time (8 PM to 6 AM) periods there. For consistency between observed average PSDs and PSDs modeled from average wind fields, average $U_{10,i}$-values are calculated at each grid point $i$ of the wind dataset as $\langle U_{10,i}\rangle = \sqrt{\left(\sum_{p=1}^{n} U_{10,i,p}^2\right)/n}$, where $n$ corresponds to the number of wind-field configurations that have local-wind-speed values lying within the same bin.

Fig. 4 shows the average wind fields computed surrounding ALOHA and KIP and at local wind speeds of 2 and 14 m/s, and Fig. 5 shows the average PSDs observed at all considered stations and for the various local wind speeds (see continuous lines). The direct relationship between observed noise power and local wind speed is obvious for all stations in the 0.5–1.5 Hz frequency range (i.e. periods of 0.6–2 s), while this is no longer the case at lower frequencies (around 0.2 Hz) where similar noise levels are observed for different local wind speeds (with the exception of the very high wind-speed cases).

In order to find the parameter values that best fit the data over all local wind speeds, we perform a grid search over all model parameter space. For each model parameter combination and each local wind speed value, we calculate the misfit (in dB) between the observed and predicted power averaged in the 0.5 to 1.5 Hz frequency band. The power averaging is done in dB space and using log-binned frequencies so that the power values are equally weighted for all frequencies within the 0.5 to 1.5 Hz range. We finally obtain the total misfit by summing misfits over all wind speeds and all seismic and acoustic observations. The total misfit values from jointly analyzing ALOHA and KIP are shown in Fig. 6(a). 5-unit bin sizes have been used for our grid search on $Q_g$, but slices are only shown every 25 units in Fig. 6(a) for clarity. A unique minimum misfit is obtained at $I = -28$ dB, $Q_w = 800$ and $Q_g = 75$. We discuss the consistency of our inverted $I$-values with previous work in Section 6.2. The quality factors $Q_w$ and $Q_g$ are of similar order of magnitude compared to those proposed in previous work. Anderson and Hough (1984) suggested $Q_g = 20$ at similar frequencies, and Gualtieri et al. (2013) proposed $Q_g \approx 35$

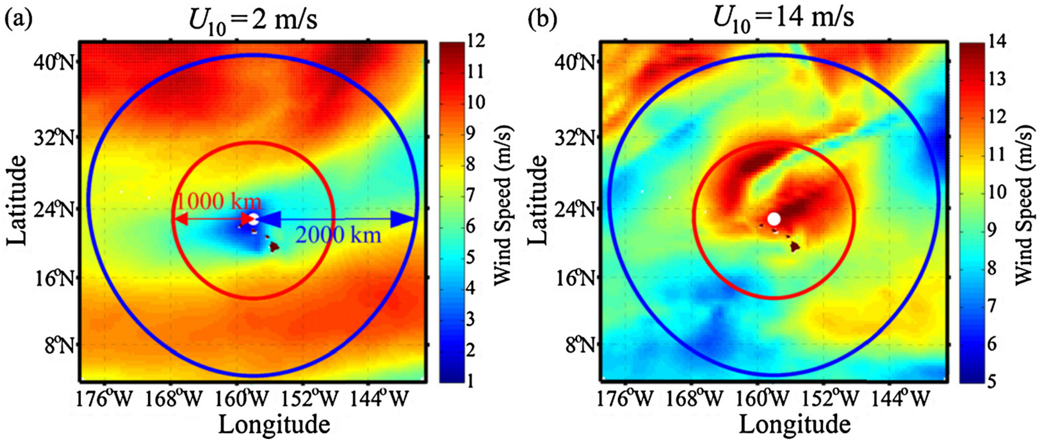

**Fig. 4.** Average wind fields computed in the Pacific Ocean from Feb. 2007 to Oct. 2008 for local-wind speeds of (a) 2 m/s and (b) 14 m/s. The white dot on each plot indicates the location of the WHOTS buoy (which we use as a wind reference in the Pacific Ocean) and the red and blue circles denote distances of 1000 and 2000 km from the WHOTS buoy. (For interpretation of the references to color in this figure legend, the reader is referred to the web version of this article.)

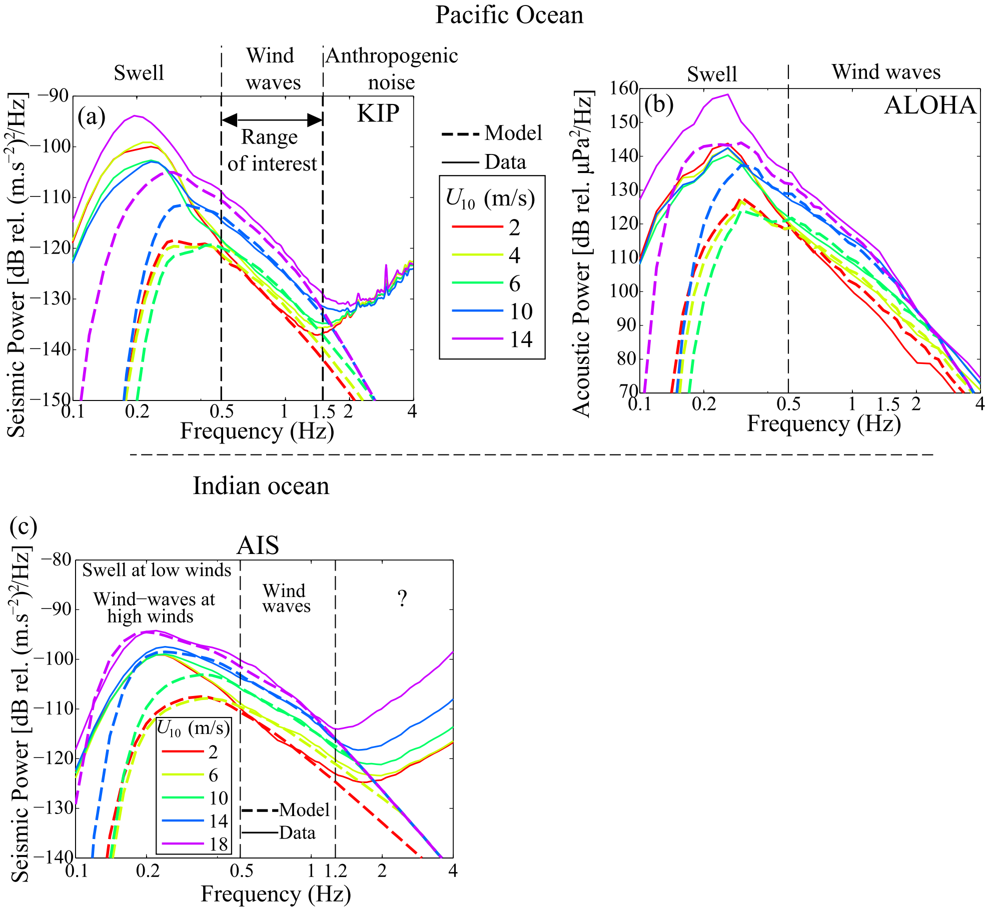

**Fig. 5.** Observed vs. modeled seismic and acoustic PSDs at (a) KIP, (b) ALOHA and (c) AIS. Continuous lines show observations and dashed lines show model predictions. The vertical dashed lines delimit the frequency bands over which seismic power is averaged for the misfit calculations shown in Fig. 6 and for the timeseries shown in Figs. 7 and 8. The red and purple lines in Fig. 5(a) for KIP and Fig. 5(b) for ALOHA are for wind speeds that correspond to the average wind fields shown in Fig. 4. (For interpretation of the references to color in this figure legend, the reader is referred to the web version of this article.)

based on noise amplitude analysis at lower frequencies. Gualtieri et al. (2013) also obtained $Q_w$-values ranging from 500 to 2000 from modeling surface waves that propagate in ocean covered areas with similar ocean depths.

We perform a similar grid search for AIS. However, since we lack acoustic measurements there, we evaluate model misfit only with respect to seismic observations. Furthermore, since AIS is located very close (about 1 km) to the ocean, $Q_g$ only weakly affects the seismic signal and is thus not well constrained in our grid search. Thus, we impose $Q_g$ to be similar to that at KIP, and set $Q_g = 75$. By performing our grid search over the 2 model parameters $I$ and $Q_w$, we obtain $I = -26$ dB and $Q_w = 1500$ (see Fig. 6(b)). The value of $I$ inverted at AIS is slightly larger than that at KIP, and we suggest that this difference could be due to more heterogeneous winds in the Indian Ocean (see Section 5). The value of $Q_w$ is about twice as large as that at KIP, which could be

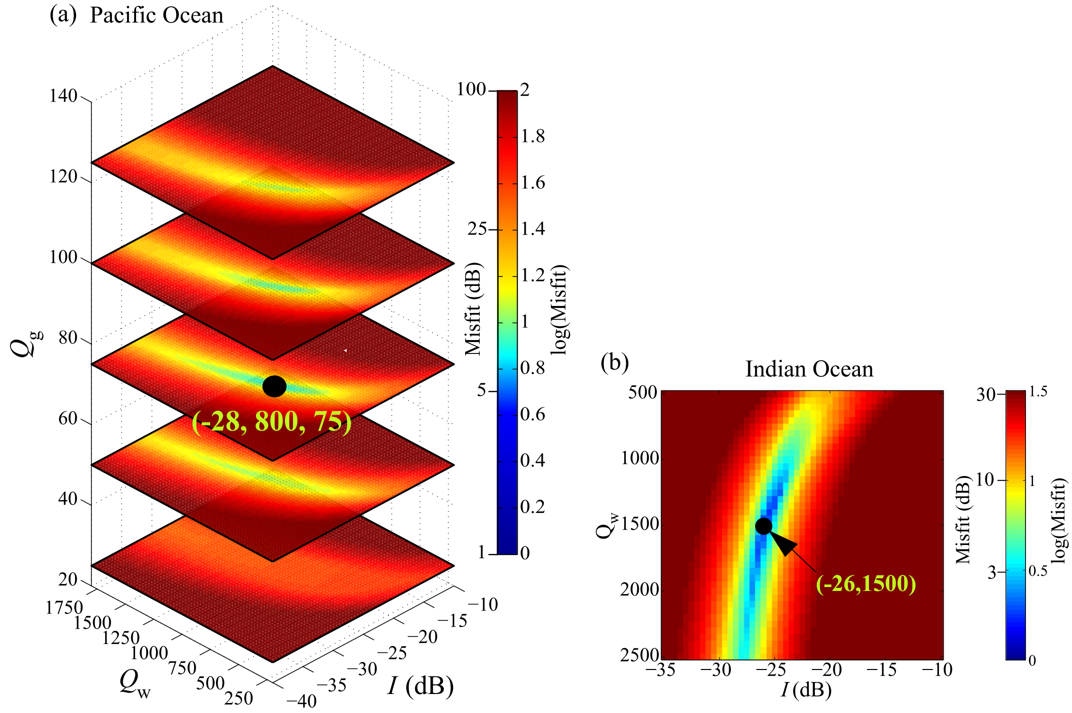

**Fig. 6.** Model misfit for various values of the model parameters $I$, $Q_w$ and $Q_g$ in (a) the Pacific Ocean (stations KIP and ALOHA) and (b) the Indian Ocean (station AIS). The minimum misfit values are highlighted by the black dots on each plot, and the corresponding modeled PSDs are shown against observations in Fig. 5(a) for KIP and (b) for ALOHA (using $I = -28$ dB, $Q_w = 800$ and $Q_g = 75$), and in Fig. 5(c) for AIS (using $I = -26$ dB, $Q_w = 1500$ and $Q_g = 75$).

due to differences in ocean floor properties between the two regions. It is important to note, though, that a significant tradeoff is obtained in Fig. 6 between $Q_w$ and $I$ at both KIP and AIS. This implies that $I$-values within ±1.5 dB of those inverted here accompanied with $Q_w$-values within a factor of about 1/3 of those inverted here would still predict the average spectra shown in Fig. 5 reasonably well. The next section shows model predictions of average PSDs and timeseries using the model-parameter values constrained here.

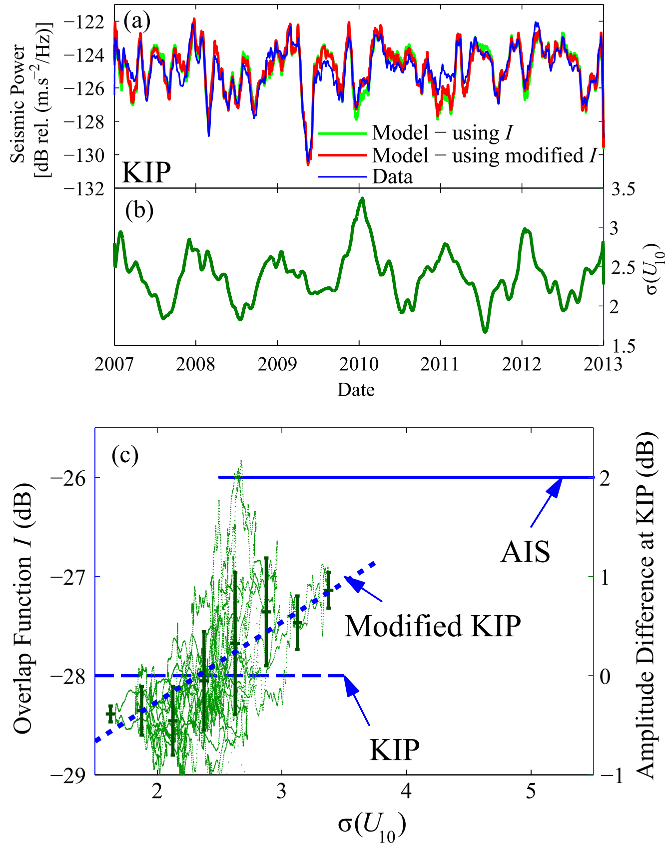

**Fig. 7.** (a) Observed (blue line) versus predicted (green and red lines) timeseries of ground acceleration power over the 2007 to 2012 time period at KIP. The green line is obtained using $I = -28$ dB as inferred in Fig. 6, while the red line is obtained using $I_{mod}$ (see equation (18)) as empirically defined in Fig. 7(c). (b) Timeseries of the standard deviation $\sigma$ of the wind values $U_{10}$ lying within a disk of 2000-km radius around the KIP station (see Fig. 4). (c) Overlap function $I$ (blue lines) and amplitude difference (green dots) between modeled and observed timeseries at KIP. The dashed and continuous blue lines show average $I$-values as inferred in Fig. 6 for KIP and AIS. The green crosses show the average of the green dots over binned values of $\sigma(U_{10})$, and the errorbars correspond to the standard deviation. We interpret the observed amplitude difference in terms of variations of the overlap function $I$ with $\sigma(U_{10})$, which we account for in the final model predictions by empirically defining the modified overlap function $I_{mod}$ as shown here by the dotted blue line. (For interpretation of the references to color in this figure legend, the reader is referred to the web version of this article.)

## 5. Results

The predicted average PSDs are shown against observations for the various local wind speeds in Fig. 5. The frequency scaling and variability with local wind speed for both the acoustic and seismic power are well represented by our wind-wave-induced noise model. Good agreement between observed and predicted PSDs is obtained from 0.5 to 4 Hz at ALOHA, from 0.5 to 1.5 Hz at KIP and from 0.5 to 1.2 Hz at AIS. The smaller frequency range of agreement between our model and the seismic observations compared to the acoustic observations at ALOHA is likely due to other noise sources overwhelming that of wind-waves at higher frequencies. This extra source is likely anthropogenic at KIP but is unknown at AIS (see Fig. S2). Interestingly, one can clearly see at station KIP and ALOHA that the noise content caused by the large swell in the Pacific Ocean is generally distinct from that of wind-waves. In contrast, wind-waves formed at high local wind speeds entirely ex-

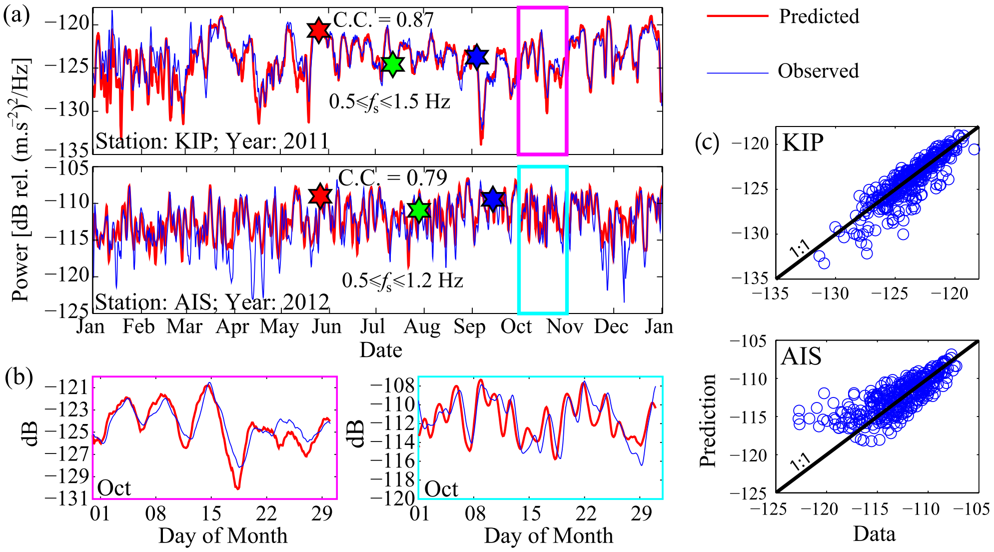

**Fig. 8.** Predicted (thick red lines) vs. observed (thin blue lines) ground acceleration power timeseries at KIP and AIS over (a) the year and over (b) the month of October (see colored rectangles in Fig. 8(a)). Colored stars in Fig. 8(a) correspond to randomly selected days over which associated PSDs are averaged and shown in Fig. 9. Fig. 8(c) shows scatter plots of predicted vs. observed noise power for the yearly predictions, where each dot corresponds to a single day. The black line indicates the 1-to-1 correspondence. (For interpretation of the references to color in this figure legend, the reader is referred to the web version of this article.)

plain the seismic energy observed in the swell frequency range at AIS. We interpret this as a result of ocean swell being smaller in the Indian Ocean due to more unsteady winds there, which allows wind-wave-induced noise to overwhelm that of swell under high local winds.

Fig. 7(a) shows the observed (blue) versus predicted (green) seismic noise timeseries at station KIP during the 2007–2012 time period. Here acceleration power has been averaged over a timescale of one week and within the 0.5–1.5 Hz frequency range (see Fig. 5(a)). Consistently good agreement is obtained between observations and predictions. However, a weak but significant mismatch can be seen between predictions and observations during the winter, i.e. during time periods for which the wind field is relatively more heterogeneous (see supplementary video). We crudely estimate the degree of heterogeneity of the wind field by evaluating the standard deviation $\sigma(U_{10})$ of the wind values that occur within 2000 km of KIP, i.e. within the red circle shown in Fig. 4. This measure is obviously not a physical nor a generic measure (for example it depends on the wind-mesh resolution), but it provides a qualitative estimate of the relatively more heterogeneous wind fields in winter (see Fig. 7(b)). The proportionality between model mismatch and $\sigma(U_{10})$ is shown in Fig. 7(c), where a linear scaling is obtained between the observed-to-predicted amplitude difference and the wind standard deviation $\sigma(U_{10})$. However, it should be noted that because the wind standard deviation $\sigma(U_{10})$ is correlated to the wind average, the deviations between observed and predicted average spectra in Fig. 6, although weak, could explain part of the observed amplitude difference versus $\sigma(U_{10})$ in Fig. 7(c).

We interpret the dependence of the amplitude difference between predictions and observations on the wind standard deviation to result from a dependence of the overlap function $I$ on the degree of wind heterogeneity. The more heterogeneous the wind field is, the more isotropic the generated seas are expected to be, and thus the larger the average overlap function $I$ is expected to be over the region that the seismic station is sensitive to. With this interpretation, we replace the constant $I$-value of −28 dB obtained in the previous section at KIP by a modified function $I_{mod}$ that has a slight dependence on the wind standard deviation $\sigma(U_{10})$. From fitting the amplitude difference observed in Fig. 7(c), we obtain

$$I_{mod} = -29.87 + 0.80\sigma(U_{10}). \tag{18}$$

Such a minor modification of the overlap function allows us to correct for the amplitude differences observed at extreme values of $\sigma(U_{10})$ at KIP (see red curve in Fig. 7(a)). We also suggest that the relatively larger average value of $I = -26$ dB inferred at AIS is caused by the more heterogeneous wind there (see supplementary video), where $\sigma(U_{10})$-values are significantly higher than for KIP but no dependence of $I$ is observed with $\sigma(U_{10})$.

Fig. 8(a) shows timeseries of ground acceleration power averaged daily and in the appropriate frequency bands, i.e. 0.5–1.5 Hz for KIP and 0.5–1.2 Hz for AIS (see Fig. 5). An overall good agreement is obtained over the year between observations and predictions, with correlation coefficients of 0.87 at KIP and 0.79 at AIS between the observed and predicted power (see scatter plots in Fig. 8(c)). We note, though, that the minimum noise levels at AIS are significantly overestimated by our model predictions. This could be due to an overestimate of $Q_w$ in Fig. 6, or to a complex dependence of $I$ with wind spatial heterogeneity. However, ground acceleration power remains reasonably well predicted at shorter timescales as shown in Fig. 8(b), which shows that the observed daily to weekly fluctuations in ground acceleration power are nicely captured by the model (see Fig. 8(b)). At even shorter timescales, there exists a slight time delay between predicted and observed noise timeseries. While predictions are always ahead of observations, the time lag is not constant over the year and can vary from 0 to 9 h. As already suggested by Duennebier et al. (2012), this time delay likely results from our crude assumption that ocean waves fully develop instantaneously, while a time delay is expected in reality (see Section 3.1). We attribute time periods of significantly larger time delays to time periods at which relatively higher wind speeds (either local or distant) mainly contribute to the resulting noise.

Finally, observed and modeled seismic PSDs are shown in Fig. 9 for 3 randomly selected days corresponding to the colored stars shown in Fig. 8(a). One can see that the daily noise spectral content as well as its variations due to temporal changes in the wind-field spatial structure is relatively well captured by the model.

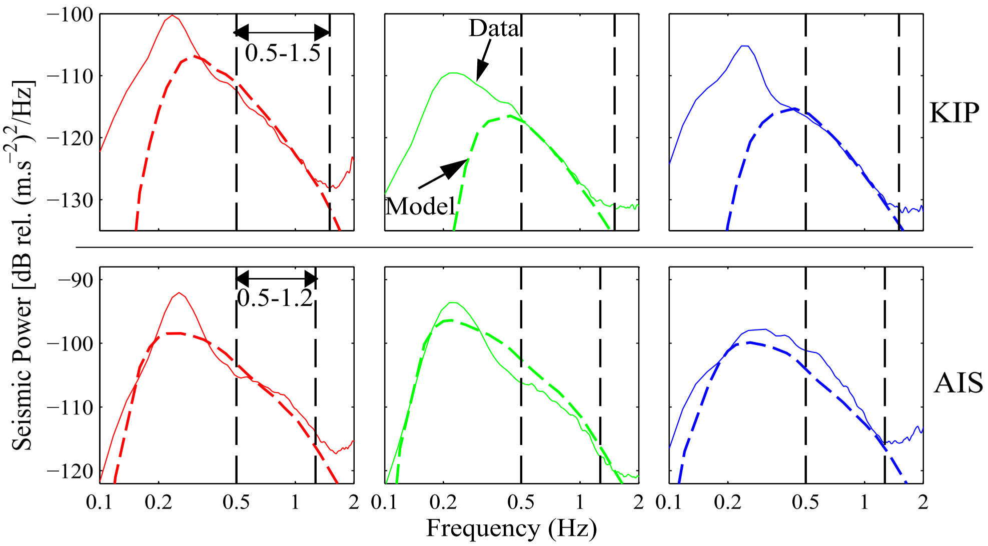

**Fig. 9.** Observed (continuous lines) versus modeled (dashed lines) daily-averaged PSDs at KIP (top) and AIS (bottom). Each panel corresponds to the randomly selected times shown by stars in Fig. 8(a) (with corresponding colors). The vertical dashed lines delimit the frequency bands over which seismic power is averaged for the timeseries shown in Figs. 7 and 8.

## 6. Discussion

### 6.1. Uncertainties on inverted model parameters

Due to our imperfect knowledge of OSGWs and ground properties, several assumptions and approximations have been made. Mainly, we assumed that wind waves are always fully developed, we modeled the crust as a homogeneous half space of constant shear-wave speed $\beta_c = 2600$ m/s with no sediment layer, and we did not account for energy loss and 3D effects as seismic waves propagate across the ocean–continent boundary.

Previous numerical modeling of Ardhuin et al. (2013) suggests that the PSD $E(f)$ obtained under non-fully developed situations can be up to 2 dB smaller than that predicted in the fully developed case. Thus, accounting for non-fully developed waves could cause values of $I$ to be up to 3.5 dB larger than those presently obtained. Uncertainties in ground structure (crustal and sediment properties) typically introduce a −3 dB to +4 dB uncertainty in the predicted noise power (see Fig. 3). Under the reasonable assumption of spatially homogeneous crustal and sediment properties nearby stations, this uncertainty should have limited effect on $Q_w$ and $Q_g$, and should entirely translates into a −4 to +3 dB uncertainty in the overlap function $I$. Energy loss at the ocean–continent boundary is unlikely to cause any bias in our inverted $I$-values, since $I$ is obtained so that the amplitude of ocean bottom pressure is reproduced at ALOHA. Instead, significant energy loss at the ocean–continent boundary would artificially lower our inverted $Q_g$-values. Interestingly though, the value of $Q_g = 75$ obtained here is not unexpectedly low as compared to values suggested in other studies (Anderson and Hough, 1984; Gualtieri et al., 2013). By considering the extreme case where no attenuation occurs in continental areas (i.e. $Q_g = \infty$), the reduction of seismic power due to energy loss at the ocean–continent boundary can be estimated to be at most 3 dB. However, such an estimate could be biased by our neglect of the difference between the ocean floor and the continent in the Green's function (Tanimoto, 2013). By assuming that uncertainties on $I$ add randomly between those due to uncertainties in the wave spectrum amplitude (+3.5 dB) and those due to uncertainties in the ground structure (−4 dB to +3 dB), we conclude that the $I$-values can potentially lie between −33 dB and −21 dB in the most extreme scenario, but with one-sigma uncertainties ranging from perhaps more like −30 to −23 dB.

### 6.2. The overlap function I and implications for the directionality of wind-waves

The $I$-values inverted here (approximately −28 and −26 dB for the chosen model parameters but potentially as low as −33 or as high as −21 dB including all model uncertainties) are significantly smaller than those of −23 to −8 dB inferred by Duennebier et al. (2012) and of −21 to −18 dB inferred by Ardhuin et al. (2013) in a similar frequency range and for similar wind speeds (see Fig. 10). This difference has two main origins. First, as in Ardhuin et al. (2013), we account for finite ocean depth. Since it is surrounded by an ocean of large extent, the acoustic noise at ALOHA from ocean-induced ground vibrations due to distant sources overwhelms by about an order of magnitude that from direct waves, which causes a decrease in $I$ by about 10 dB as compared to the infinitely deep ocean case considered by Duennebier et al. (2012). Second, we use the equilibrium-range scaling, which causes an extra 5 to 10 dB decrease in $I$ as compared to the previous estimates of Ardhuin et al. (2013) due to larger OSGW amplitudes predicted at higher frequencies (see Fig. 2). Use of the equilibrium-range scaling should be appropriate since it is an inherent feature of OSGW spectra (Forristall, 1981; Kahma, 1981; Hwang and Wang, 2001; Long and Resio, 2007), and is theoretically supported by the occurrence of wave–wave interactions (Hasselmann, 1962; Kitaigorodskii, 1983). Interestingly, our representation of the equilibrium range allows us to capture the acoustic observations at ALOHA without involving complex variations in the overlap function $I$ with wind speed as suggested by Duennebier et al. (2012), which as yet has no theoretical justification.

To test whether our inverted $I$-values are consistent with previous observations of directional OSGW spectra, we use the previous parametrization proposed by Ewans (1998), which describes the directional function $M(f,\theta)$ for wind-waves (see equation (2)) using a double Gaussian function

$$M(f,\theta) = \frac{1}{\sqrt{8\pi}\sigma(f)}\left\{\exp\left[-\frac{1}{2}\left(\frac{\theta-\theta_1}{\sigma(f)}\right)\right] + \exp\left[-\frac{1}{2}\left(\frac{\theta-\theta_2}{\sigma(f)}\right)\right]\right\}, \quad (19)$$

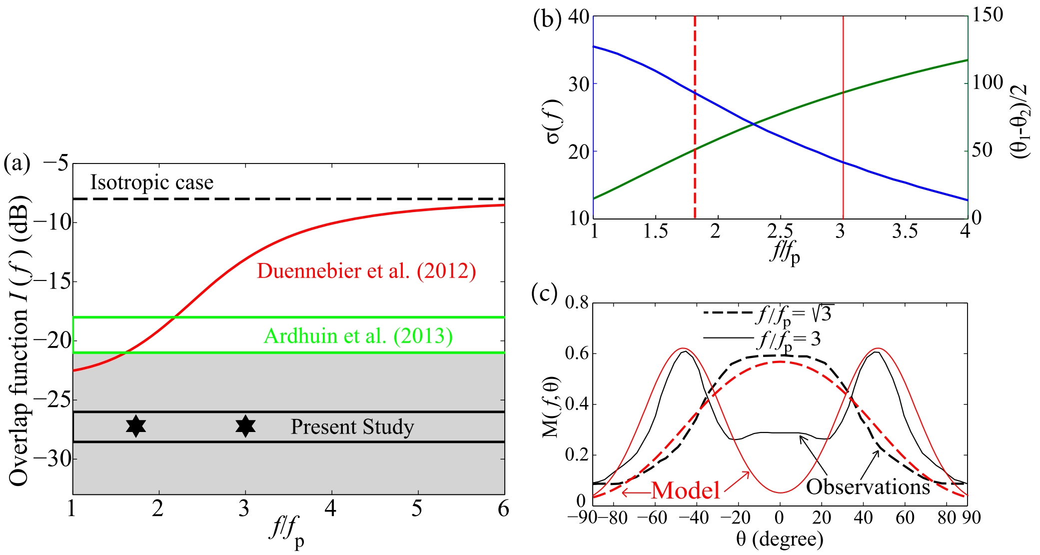

**Fig. 10.** Directional properties of the OSGWs associated with our average inverted $I$-value of $-27$ dB. (a) $I$-values inverted in our study as compared to those inverted from acoustic noise in the previous studies of Duennebier et al. (2012) and Ardhuin et al. (2013). These studies both inverted $I$ at ALOHA, i.e. for similar 2 to 16 m/s wind speeds, and $I$-values have been taken in a similar frequency range (0.5 to 1.5 Hz). The grey region indicates the range of possible $I$-values including all model uncertainties. Black stars indicate the configurations shown in Fig. 10(c). (b) Standard deviation $\sigma(f)$ (blue line) and angle difference $(\theta_1-\theta_2)/2$ (green line) associated with the double-Gaussian formulation of equation (19). The angle difference $(\theta_1-\theta_2)/2$ is set from the formulation of Ewans (1998) (see equation (20)), while $\sigma(f)$ is inverted such that our average value of $I=-27$ dB is obtained (see Fig. 10(a)). Vertical dashed and dotted lines indicate the configurations shown in (c). (c) Directional function $M(f,\theta)$ as a function of $\theta$ for frequencies $f=\sqrt{3}f_p$ (dashed lines) and $f=3f_p$ (continuous lines) as inverted in this study (red) and as observed by Hwang et al. (2000) (black). (For interpretation of the references to color in this figure legend, the reader is referred to the web version of this article.)

where $\sigma(f)$ corresponds to the standard deviation of each Gaussian and $\theta$ corresponds to the direction of wave propagation with respect to the local wind direction, with $\theta_1$ and $\theta_2$ being the average values of each Gaussian distribution defined as

$$\theta_2=-\theta_1=\frac{1}{2}\exp\left[5.453-2.750\left(\frac{f}{f_p}\right)^{-1}\right]. \tag{20}$$

This bimodal description of OSGW directionality was first proposed on the basis of inversions of directional buoy records (Ewans, 1998), but has since been supported by various observations that use different techniques, including airborne imagery (Hwang and Wang, 2001; Hwang et al., 2000). The increasing departure of wave propagation direction from wind direction as frequency increases is thought to result from wave–wave interactions (Banner and Young, 1994). Good observational constraints exist on the amplitude of the angle difference between the two Gaussian distributions, i.e. on $\theta_1-\theta_2$, for frequencies ranging from $1f_p$ to $4f_p$ (see green line in Fig. 10(b)). In contrast, the standard deviation $\sigma(f)$ defined in equation (19) is poorly constrained and inverted values for it strongly depend on the observational and inversion methods (Ewans, 1998). We thus use $\sigma(f)$ as a tuning parameter to obtain our central value of $I=-27$ dB, and then compare the obtained directional function $M(f,\theta)$ with those previously reported. The values of $\sigma(f)$ as inverted by substituting equations (19) and (20) into equation (2) are shown in Fig. 10(b). In contrast to the suggestion of Ewans (1998), we obtain a standard deviation $\sigma(f)$ that decreases with frequency, i.e. the directional distribution of each lobe narrows with frequency. This could be explained by the canceling of waves in certain azimuthal directions due to wave–wave interactions. The directional function $M(f,\theta)$ inferred from our inversions is shown against the previous observations of Hwang et al. (2000) in Fig. 10(c) for two selected non-dimensional frequencies $f/f_p=\sqrt{3}$ and $f/f_p=3$. We obtain good agreement between observed and modeled $M(f,\theta)$-functions for both frequencies. We thus conclude that previously reported $M(f,\theta)$-functions remain consistent with our inverted $I$-values. It is important to note that the larger values of $M(f,\theta)$ observed by Hwang et al. (2000) at $f/f_p=3$ and in the $-30$ to $+30$ degrees angle range as compared to our inverted values do not significantly affect the associated $I$-values. In fact, the detailed shape of the $M(f,\theta)$-function from $-90$ to 90° with respect to wind direction is not sufficient to provide good constraints on $I$, and reliable observations of $M(f,\theta)$ at $\theta$-values from $-180$ to $-90°$ and from 90 to 180° are needed. As an example, the relatively larger values observed by Hwang et al. (2000) at ±90° as compared to those inverted here (see Fig. 10(c)) would be sufficient to cause $I$-values to be 10 to 20 dB larger than $-27$ dB if they were to remain as large for all angles in the opposite-wind direction, i.e. for $\theta$-values smaller than $-90°$ or larger than 90°. Unfortunately, Hwang et al. (2000) were not able to solve for $M(f,\theta)$ in these wind-opposite directions, since the direction of ocean wave propagation could not be solved for from airborne imagery. In addition, measurements of realistic and accurate values of $M(f,\theta)$ in this angle range are likely to be challenging to obtain from classical devices due to the poor signal-to-noise ratio expected within this angle range.

### 6.3. *Applications*

We expect our modeling framework to be particularly useful for monitoring sea-ice and for correcting noise correlation measurements from source directivity effects. In the context of the shrinking sea ice cover observed in recent years in the Arctic basin, the marginal ice zones of the ice pack are increasingly affected by storm-generated waves that break-up the ice (Kohout et al., 2014). Increasing ocean wave heights and the reduction of sea ice mechanical strength (Gimbert et al., 2012) are major controls on sea ice disintegration, but the scientific community currently lacks observational tools from which ocean waves and their relation with ice-cover mechanical strength can be continuously monitored. Tsai and McNamara (2011) suggested that sea-ice mechanical strength could be monitored from land-based seismic stations through the damping of ground motion power observed in the 0.6–2 s period range. The framework presented here can now be used to assess wave-amplitude changes due to sea ice from seismic noise, which one could translate to changes in sea ice mechanical strength by developing appropriate mechanical models.

More generally, we also expect our framework to be useful in the context of the growing use of dense seismic arrays for high-resolution tomography from noise correlation techniques (e.g. Bowden et al., 2015). These noise tomography techniques typically rely on the assumption of isotropic noise sources distributed around stations, which is rarely true in reality (Tsai, 2009; Fichtner, 2014). In particular, it is common that dense seismic arrays are placed in coastal regions (e.g. the Long Beach array, California, see Lin et al., 2013), and are thus mainly sensitive to seismic noise incoming from a single side of the network, i.e. within ±90° of azimuth (Bowden et al., 2015). The effect of anisotropic noise sources could be determined using our model, therefore improving the ability of noise correlation studies to obtain robust results.

## 7. Conclusions

We have shown that ocean-floor acoustic and near-coastal seismic noise measurements can simultaneously be modeled in the 0.6–2 s period band. This shows that deep-water and near-shore secondary-microseism sources are sufficient to explain the seismic noise characteristics (amplitude, frequency scaling) observed in coastal regions. There is thus no need to include other source contributions like the breaking of ocean waves on the shore as suggested by Beucler et al. (2014). We suggest that the fraction of ocean waves traveling in nearly-opposite directions is smaller than previously proposed, but still consistent with the available direct observations. We expect the direct and robust relationship reported herein between seismic noise content in coastal regions and local wind-wave properties to be useful for various applications, such as for the remote monitoring of sea ice mechanical properties and for correcting noise-correlation measurements for source directivity.

## Acknowledgements

This study was partially funded by Stanback Discovery Fund for Global Environmental Science and NSF grant EAR-1453263. We thank two anonymous reviewers for helpful reviews.

## Appendix A. Supplementary material

Supplementary material related to this article can be found online at http://dx.doi.org/10.1016/j.epsl.2015.06.017.

## References

Aki, K., Richards, P.G., 2002. Quantitative Seismology, 2nd edition. Univ. Sci. Books, Sausalito, Calif. 700 pp.

Alves, J.H.G.M., Banner, M.L., Young, I.R., 2003. Revisiting the Pierson–Moskowitz asymptotic limits for fully developed wind waves. J. Phys. Oceanogr. 33 (7), 1301–1323.

Anderson, J.G., Hough, S.E., 1984. A model for the shape of the Fourier amplitude spectrum of acceleration at high frequencies. Bull. Seismol. Soc. Am. 74 (5), 1969–1993.

Ardhuin, F., Gualtieri, L., Stutzmann, E., 2015. How ocean waves rock the Earth: two mechanisms explain microseisms with periods 3 to 300 s. Geophys. Res. Lett. 42 (3) 2014GL062782.

Ardhuin, F., Herbers, T.H.C., 2013. Noise generation in the solid Earth, oceans and atmosphere, from nonlinear interacting surface gravity waves in finite depth. J. Fluid Mech. 716, 316–348.

Ardhuin, F., Lavanant, T., Obrebski, M., Mari, L., Royer, J.-Y., d'Eu, J.-F., Howe, B.M., Lukas, R., Aucan, J., 2013. A numerical model for ocean ultra-low frequency noise: wave-generated acoustic-gravity and Rayleigh modes. J. Acoust. Soc. Am. 134 (4), 3242–3259.

Banner, M.L., Young, I.R., 1994. Modeling spectral dissipation in the evolution of wind waves. Part I. Assessment of existing model performance. J. Phys. Oceanogr. 24 (7), 1550–1571.

Battjes, J.A., Zitman, T.J., Holthuusen, L.H., 1987. A reanalysis of the spectra observed in JONSWAP. J. Phys. Oceanogr. 17 (8), 1288–1295.

Berger, J., Davis, P., Ekstrm, G., 2004. Ambient Earth noise: a survey of the global seismographic network. J. Geophys. Res., Solid Earth 109 (B11), B11307.

Beucler, E., Mocquet, A., Schimmel, M., Chevrot, S., Quillard, O., Vergne, J., Sylvander, M., 2014. Observation of deep water microseisms in the north Atlantic ocean using tide modulations. Geophys. Res. Lett. 2014GL062347.

Bowden, D.C., Tsai, V.C., Lin, F.C., 2015. Site amplification, attenuation and scattering from noise correlation amplitudes across a dense array in Long Beach, CA. Geophys. Res. Lett. 2014GL062662.

Campillo, M., Paul, A., 2003. Long-range correlations in the diffuse seismic coda. Science 299 (5606), 547–549.

Dee, D.P., Uppala, S.M., Simmons, A.J., Berrisford, P., Poli, P., Kobayashi, S., Andrae, U., Balmaseda, M.A., Balsamo, G., Bauer, P., Bechtold, P., Beljaars, A.C.M., van de Berg, L., Bidlot, J., Bormann, N., Delsol, C., Dragani, R., Fuentes, M., Geer, A.J., Haimberger, L., Healy, S.B., Hersbach, H., Hólm, E.V., Isaksen, L., Kållberg, P., Köhler, M., Matricardi, M., McNally, A.P., Monge-Sanz, B.M., Morcrette, J.-J., Park, B.-K., Peubey, C., de Rosnay, P., Tavolato, C., Thépaut, J.-N., Vitart, F., 2011. The ERA-Interim reanalysis: configuration and performance of the data assimilation system. Q. J. R. Meteorol. Soc. 137 (656), 553–597.

Donelan, M.A., Hamilton, J., Hui, W.H., 1985. Directional spectra of wind-generated waves. Philos. Trans. R. Soc. Lond. Ser. A, Math. Phys. Sci. 315 (1534), 509–562.

Duennebier, F., Harris, D., Jolly, J., 2008. ALOHA cabled observatory will monitor ocean in real time. Sea Technol. 49, 51–54.

Duennebier, F.K., Lukas, R., Nosal, E.-M., Aucan, J., Weller, R.A., 2012. Wind, waves, and acoustic background levels at station ALOHA. J. Geophys. Res., Oceans 117 (C3), C03017.

Ewans, K.C., 1998. Observations of the directional spectrum of fetch-limited waves. J. Phys. Oceanogr. 28 (3), 495–512.

Farrell, W.E., Munk, W., 2008. What do deep sea pressure fluctuations tell about short surface waves? Geophys. Res. Lett. 35 (19), L19605.

Fichtner, A., 2014. Source and processing effects on noise correlations. Geophys. J. Int. 197, 1527–1531.

Forristall, G.Z., 1981. Measurements of a saturated range in ocean wave spectra. J. Geophys. Res., Oceans 86 (C9), 8075–8084.

Gimbert, F., Jourdain, N.C., Marsan, D., Weiss, J., Barnier, B., 2012. Recent mechanical weakening of the Arctic sea ice cover as revealed from larger inertial oscillations. J. Geophys. Res., Oceans 117 (C11), C00J12.

Gualtieri, L., Stutzmann, E., Capdeville, Y., Ardhuin, F., Schimmel, M., Mangeney, A., Morelli, A., 2013. Modelling secondary microseismic noise by normal mode summation. Geophys. J. Int. 193, 1732–1745.

Hamilton, E.L., 1976. Shear-wave velocity versus depth in marine sediments; a review. Geophysics 41 (5), 985–996.

Hasselmann, K., 1962. On the non-linear energy transfer in a gravity-wave spectrum. Part 1. General theory. J. Fluid Mech. 12 (04), 481–500.

Hasselmann, K., 1963. A statistical analysis of the generation of microseisms. Rev. Geophys. 1 (2), 177–210.

Hasselmann, K., Sell, W., Ross, D.B., Mller, P., 1976. A parametric wave prediction model. J. Phys. Oceanogr. 6 (2), 200–228.

Herrmann, R.B., 2013. Computer programs in seismology: an evolving tool for instruction and research. Seismol. Res. Lett. 84 (6), 1081–1088.

Holthuijsen, L.H., 2010. Waves in Oceanic and Coastal Waters, 1st edition. Cambridge University Press, Cambridge.

Hwang, P.A., Wang, D.W., 2001. Directional distributions and mean square slopes in the equilibrium and saturation ranges of the wave spectrum. J. Phys. Oceanogr. 31 (5), 1346–1360.

Hwang, P.A., Wang, D.W., Walsh, E.J., Krabill, W.B., Swift, R.N., 2000. Airborne measurements of the wavenumber spectra of ocean surface waves. Part II. Directional distribution. J. Phys. Oceanogr. 30 (11), 2768–2787.

Kahma, K.K., 1981. A study of the growth of the wave spectrum with fetch. J. Phys. Oceanogr. 11 (11), 1503–1515.

Kedar, S., Longuet-Higgins, M., Webb, F., Graham, N., Clayton, R., Jones, C., 2008. The origin of deep ocean microseisms in the north Atlantic ocean. Proc. R. Soc., Math. Phys. Eng. Sci. 464 (2091), 777–793.

Kitaigorodskii, S.A., 1983. On the theory of the equilibrium range in the spectrum of wind-generated gravity waves. J. Phys. Oceanogr. 13 (5), 816–827.

Kohout, A.L., Williams, M.J.M., Dean, S.M., Meylan, M.H., 2014. Storm-induced sea-ice breakup and the implications for ice extent. Nature 509 (7502), 604–607.

Lin, F.-C., Tsai, V.C., Schmandt, B., Duputel, Z., Zhan, Z., 2013. Extracting seismic core phases with array interferometry. Geophys. Res. Lett. 40 (6), 1049–1053.

Long, C.E., Resio, D.T., 2007. Wind wave spectral observations in Currituck Sound, North Carolina. J. Geophys. Res., Oceans 112 (C5), C05001.

Longuet-Higgins, M., Ursell, F., 1948. Sea waves and microseisms 162, 700.

Longuet-Higgins, M.S., 1950. A theory of the origin of microseisms. Philos. Trans. R. Soc. Lond. Ser. A, Math. Phys. Sci. 243 (857), 1–35.

McGarr, A., 1969. Amplitude variations of Rayleigh waves-propagation across a continental margin. Bull. Seismol. Soc. Am. 59 (3), 1281–1305.

McNamara, D.E., Buland, R.P., 2004. Ambient noise levels in the continental United States. Bull. Seismol. Soc. Am. 94 (4), 1517–1527.

Mitsuyasu, H., Tasai, F., Suhara, T., Mizuno, S., Ohkusu, M., Honda, T., Rikiishi, K., 1975. Observations of the directional spectrum of ocean waves using a cloverleaf buoy. J. Phys. Oceanogr. 5 (4), 750–760.

Phillips, O.M., 1958. The equilibrium range in the spectrum of wind-generated waves. J. Fluid Mech. 4 (04), 426–434.

Pierson, W.J., Moskowitz, L., 1964. A proposed spectral form for fully developed wind seas based on the similarity theory of S.A. Kitaigorodskii. J. Geophys. Res. 69 (24), 5181–5190.

Plueddemann, A.J., Weller, R.A., Lukas, R., Lord, J., Bouchard, P.R., Walsh, M.A., 2006. WHOI Hawaii Ocean Timeseries Station (WHOTS): WHOTS-2 mooring turnaround cruise report. Woods Hole Oceanographic Institution, Woods Hole, MA.

Tanimoto, T., 2013. Excitation of microseisms: views from the normal-mode approach. Geophys. J. Int. 194 (3), 1755–1759.

Tsai, V.C., 2009. On establishing the accuracy of noise tomography travel-time measurements in a realistic medium. Geophys. J. Int. 178 (3), 1555–1564.

Tsai, V.C., Atiganyanun, S., 2014. Green's functions for surface waves in a generic velocity structure. Bull. Seismol. Soc. Am. 104 (5), 2573–2578.

Tsai, V.C., McNamara, D.E., 2011. Quantifying the influence of sea ice on ocean microseism using observations from the Bering Sea, Alaska. Geophys. Res. Lett. 38 (22), L22502.

Webb, S.C., 1992. The equilibrium oceanic microseism spectrum. J. Acoust. Soc. Am. 92 (4), 2141–2158.

Zhang, J., Gerstoft, P., Shearer, P.M., 2009. High-frequency P-wave seismic noise driven by ocean winds. Geophys. Res. Lett. 36 (9), L09302.